In-situ Raman mapping of Si island electrodes and stress modeling as a function of lithiation and size

Haotian Wang,[a†] Yueming Song,[b‡] Victoria Castagna Ferrari,[a] Nam Soo Kim,[c] Sang Bok Lee,[c] Paul Albertus,[b] Gary Rubloff,[a] David Murdock Stewart [a]*

[a] Department of Materials Science and Engineering & Institute for Research in Electronics and Applied Physics, University of Maryland, College Park, MD 20740, United States
[b] Department of Chemical and Biomolecular Engineering, University of Maryland, College Park, MD 20740, United States
[c] Department of Chemistry and Biochemistry, University of Maryland, College Park, MD 20740, United States

*Email: steward@umd.edu

Present Addresses:
[†] Enovate Corp. 101 Theory #200, Irvine, CA 92617, United States
[‡] Futronics Corp. 225 S. Lake Avenue, Pasadena, CA 91101, United States.

Keywords: *In-situ stress measurement, confocal Raman spectroscopy, Si electrode, Tungsten oxide lithiation, critical size effect, ECM coupling*

Abstract

Si is known for cracking and delamination during electrochemical cycling of a battery, due to the large volume change associated with Li insertion and extraction. However, it has been found experimentally that patterned Si island electrodes 200 nm thick and less than 7 μm wide can deform in a purely elastic manner. Inspired by this, we performed *in-situ* Raman stress characterization of model poly-crystalline Si island electrodes using an electrochemical cell coupled with an immersion objective lens and designed for short working distance. A 5 μm wide Si island electrode showed a parabolic stress profile during lithiation, while for a 15 μm Si island electrode, a stress plateau in the center of the electrode was observed. A continuum model with coupled electro-chemo-mechanical physics was established to understand the stress measurement. A qualitative agreement was reached between modeling and experimental data, and the critical size effect could be explained by the Li diffusive flux as governed by competition between the Li concentration and hydrostatic stress gradients. Below the critical size, the stress gradient drives Li towards the edges, where the electrode volume is free to expand, while above the critical size, the stress plateau inhibits Li diffusion to the edge and forces destructive stress relief by cracking. This work represents a promising methodology for *in-situ* characterization of electro-chemo-mechanical coupling in battery electrodes, with suggestions provided for further improvement.

Introduction

Si is a promising electrode material for Li ion battery (LIB) as it has high energy density (3600 mAh/g) and low working potential (~0.1-0.4 V vs Li/Li^+).[1] However, Si electrode is also known for its large volume change associated with lithium insertion and extraction, which creates many mechanical issues such as cracking, delamination, and pulverization. As a result, the mechanical degradation of Si electrode destroys its structural integrity and expedites the capacity fading of LIBs.[2–4] The mechanical challenges limit the application of Si electrodes in LIBs, and to overcome these issues, various novel Si electrodes, including nanoparticles, double-walled hollow tubes, core-shell, and yolk-shell structures, have been developed in

the past decade.[5–10] The nano-sized structures lead to fast Li transport and facile stress relaxation which enable Si electrodes to maintain the structural integrity over extensive electrochemical cycles. Additionally, it has been experimentally observed that nano-sized Si electrodes exhibit critical sizes, below which Si electrodes don't undergo fracture and pulverization. For Si nanoparticles, an *in-situ* TEM study has shown that the critical diameter is around 150 nm,[11] while for Si nanowires, the critical diameter is around 300 nm.[12] Similar critical size effects also occur in Si thin film electrodes,[13–15] and when the Si thin films are patterned into islands, a critical island size of 7-10 μm has been found, below which no delamination or cracking occurs.[16,17]

Various mechanical models have been proposed to account for the critical size effect in nanostructured Si electrodes,[18–22] but the stress fields derived from these models are based only on average strain states observed in a few experimental studies.[17,23–27] In one study, Soni et al. used multi-beam optical sensor to investigate the stress evolution in amorphous Si thin films.[23] It was found that the stress stabilized during lithation and delithiation, attributed to plastic flow in the a-Si thin film. Additionally, the average flow stress and the volumetric charge storage both increase as the thickness of the a-Si thin film decreases, due to facile lithiation in the thinner a-Si film. In thicker a-Si thin films, the sluggish diffusion leads to lower Li concentration towards the current collector relative to the surface, and the associated tensile stress gradient led to fracture initiation at the Si/current collector interface.[4] For thinner films, the concentration disparity is less, which explains why, below a certain thickness, a-Si thin films do not undergo cracking.

In another study, Soni et al. used the same *in-situ* multi-beam optical sensor technique to investigate the stress evolution in patterned Si thin film electrodes.[17] It was found that for square shape Si islands with a width of 17 μm, the nominal stress reached a plateau during both lithiation and delithiation steps, indicating plastic deformation, while for Si islands of 7 μm width, no stress plateau was presented, indicating absence of plastic deformation. A "shear lag" model was proposed to account for the critical size effect observed in this work, where below the critical size, Si island electrodes can undergo pure elastic deformation in the lateral plane to accommodate the excessive stress exerted by lithiation and delithiation, while above the critical size, the stress would increase from the periphery and reach a plateau in the center of Si island, causing plastic flow and shearing against the current collector.

Mechanical studies of Si nanoparticles and nanowires using *in-situ* multi-beam optical sensor, Raman, and XRD were also conducted,[24–27] but they are all limited to average stress measurement. As Sethuraman pointed out, the stress and strain fields are the root cause for any mechanical damage of Si electrodes,[28] and are also the key to explaining the outstanding performance of nanostructured Si electrodes. However, to the best of the authors' knowledge, there are no prior experimental studies that directly mapped the strain field in Si electrodes induced by electrochemical lithiation/delithiation.

Our previous study has demonstrated that micro-Raman spectroscopy is a promising technique to measure stress and resolve the stress distribution in a crystalline Si electrode.[29] Therefore, in this work, we established an experimental setup for *in-situ* Raman mapping on patterned polycrystalline Si (poly-c Si) thin film electrodes to characterize inhomogeneities in the stress field during electrochemical cycling. To enable *in-situ* confocal Raman measurement, a novel electrochemical cell along with a water immersion objective lens was used. The experimental setup showed a spatial resolution of ~500 nm. Model electrode devices of square poly-c Si islands with widths of 5 μm and 15 μm were patterned on a W current collector deposited on a Si wafer. A layer of WO_x (x~3) was inadvertently formed by air exposure during transfer between W deposition and subsequent poly-c Si. The electrochemical conversion reaction of Li_xWO_3 imposed stress (~0.7 GPa) on the poly-c Si islands, as measured by Raman mapping. By controlling the potential range in the cyclic voltammetry, we selectively lithiated WO_3 in the initial cycle and created a

stretched Li_xWO_3 substrate for the subsequent lithiation/delithiation of Si island electrodes in the following cycles.

Different stress distribution profiles were observed in the Si island electrodes with 5 μm and 15 μm widths. To analyze the experimental results, a FEA model with coupled electro-chemo-mechanical (ECM) physics was developed. The modeling results showed a qualitative agreement with experimental data, and the different stress profiles could be attributed to different stress relaxation modes in Si island electrodes at different widths. Overall, the stress field development and the understanding of ECM coupling effect obtained from this study showed a good consistency with prior literature, and the methodology presented in this work shows an intriguing route for future Raman stress characterization in Si and other battery electrode materials.

Methods

Sample fabrication

The fabrication process of patterned poly-c Si thin film electrodes consists of five steps: First, 500 nm of SiO_2 was grown on 3 in Si wafers through thermal oxidation in a furnace (Tystar, Tytan). Second, 100 nm of tungsten thin film was deposited through DC magnetron sputtering (AJA, ATC-Orion 8), using a metallic W target (99.95% purity, 2 in diameter). During sputtering, the substrate temperature was kept at room temperature and 300 W power was applied to the W target to maintain a bias voltage of ~150 V. Next, Poly-c Si thin film with 200 nm thickness was deposited on the substrate through low pressure chemical vapor deposition (LPCVD) process at 650 °C in a hot wall CVD reactor (Tystar, Tytan), with gas mixture of Silane (SiH_4) and N_2. Then, the poly-c Si thin film was patterned through photolithography using a bright field mask and positive photoresist (Shipley, 1813). Reactive ion etching (RIE) was performed in an ICP etcher (Oxford) to remove exposed poly-c Si. During the etching process, a gas mixture of 10 sccm O_2, 50 sccm Ar, and 50 sccm CF_4 flowed into the chamber, and 50 W power was applied to the RF power supply to maintain a bias voltage of ~150 V. 40 mTorr chamber pressure and 20ºC substrate temperature were maintained during the etching process.

μ-Raman spectroscopy

During Raman measurement, a 60X water immersion objective lens with NA 0.95 was used (Olympus, LUMPlanFl). 633 nm laser (HeNe) with D1 intensity filter were used, and the incident laser power was controlled to 1 mW. 400 μm hole and 100 μm slit were used for each acquisition, and 8 s exposure was chosen to maintain a balance between Raman signal intensity and destruction to lithiated poly-c Si electrode. A derivation of the strain-Raman shift relationship for our poly-c Si thin film can be found in the Supporting Information.

Scanning electron microscopy (SEM) and X-ray diffraction (XRD)

SEM was performed on a dual-beam field emission SEM system (Tescan, GAIA3) with 10 kV acceleration voltage. As-fabricated samples without patterning were characterized by XRD. Diffraction patterns were measured using Cu Kα radiation in Bragg–Brentano geometry. Bruker D8 Advance powder diffractometer (Karlsruhe, Germany) equipped with theta-2theta goniometer and LynxEye position sensitive detector was used. Data were collected from 10 to 65° 2θ with step size of 0.015° and counting time of 2 s per step. The ICDD powder diffraction database was used for XRD spectra matching.

Finite element analysis (FEA)

FEA modeling was performed using COMSOL Multiphysics with the general form PDE module. In this study, a 2D model with plane strain condition was considered. In addition, linear elastic deformation of materials and Li induced deformation, without plasticity, were included in the model. A detailed formulation of the model's constitutive equations for ECM coupling, as well as material parameters, is provided in the Supporting Information.

Results and discussion

Sample characterization and confocal Raman setup

Model devices with poly-c Si thin film island electrodes and tungsten current collectors were fabricated through a process illustrated in Figure 1a, and details of the fabrication process were elaborated in the method section. W was selected as current collector here due to its high thermal stability (melting point at 3422 °C[30]) and chemical inertness against silane at elevated temperature (Tungsten silicide formation at ~750 °C[31]). The as-fabricated model devices were examined by SEM. As shown in Figure 1b, the patterned Si island electrodes were separated from each other by 75 µm to avoid mechanical interaction between neighboring islands. The plane view SEM image of each individual Si island, as shown in Figure 1c, indicates that the patterned geometry exhibits a high resolution. Thickness of layers in the model devices was examined by cross-sectional SEM, and it is shown in Figure 1d that W and poly-c Si layers have thicknesses of ~80 nm and 200 nm, respectively.

To enable confocal Raman measurement, a water immersion objective lens, along with a custom-made electrochemical cell, were used. The components of this cell are shown in Figure 2a, and the cell body (i.e. lower and upper cell chamber) is made of high-density polyethylene (HDPE) due to its chemical inertness. In this cell, the Li counter electrode is placed in the lower cell chamber, while Si working electrode is placed in the upper chamber, to accommodate the short working distance of the water immersion objective lens

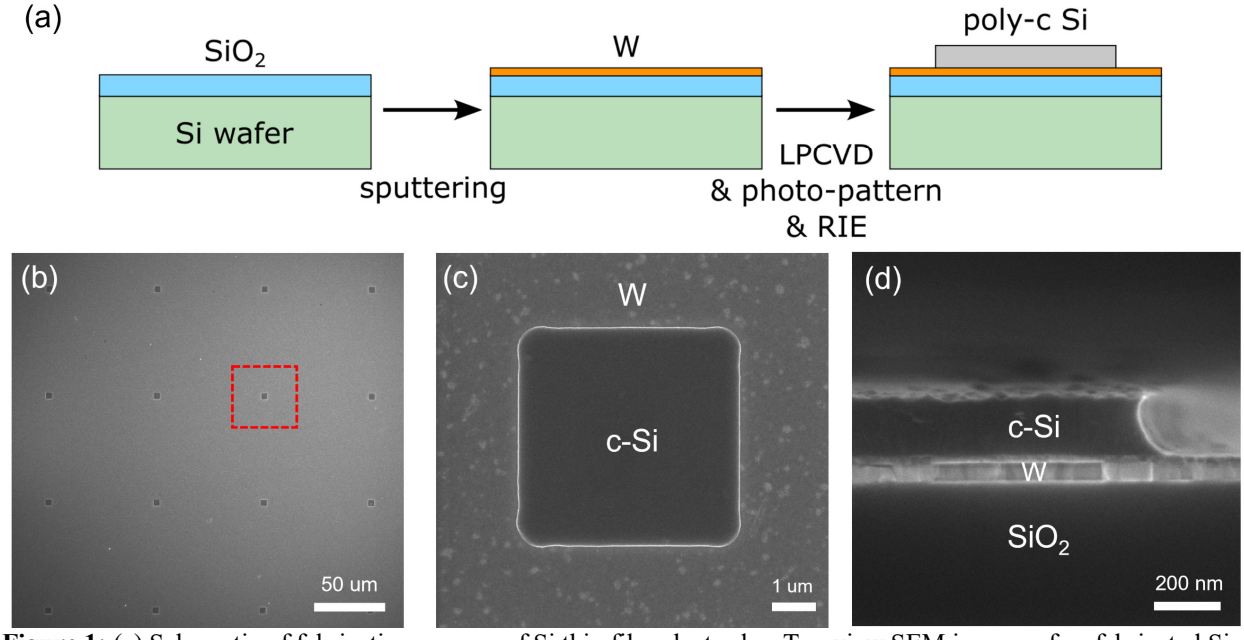

Figure 1: (a) Schematic of fabrication process of Si thin film electrodes. Top view SEM images of as-fabricated Si thin film electrodes in (b) low magnification, and (c) high magnification (image area corresponds to red dashed square in (b)). (d) Cross-sectional SEM image of as-fabricated Si electrodes.

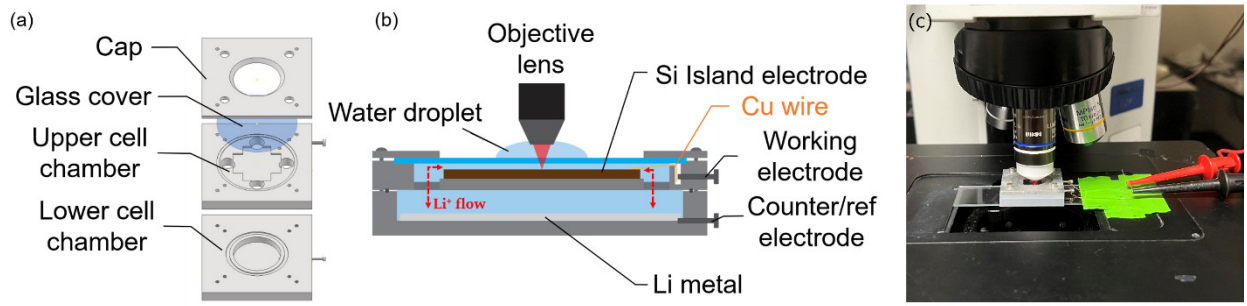

Figure 2: Schematic of (a) Homemade electrochemical cell, and (b) cross section of battery half-cell for *in-situ* Raman experiment setup. (c) Picture of *in-situ* Raman experiment.

(W.D. = 2 mm). The configuration of assembled half-cell and *in-situ* Raman experiment setup is shown in Figure 2b. Raman laser travels through water (n=1.33), borosilicate glass (n=1.48[32]), and liquid electrolyte (1 M $LiClO_4$ in propylene carbonate, n=1.44[33]) to reach the surface of Si working electrode. In this case, the refractive index of medium between Si electrode and objective lens is closely matched, and a confocal Raman measurement with reduced optical aberration is enabled.

To test the spatial resolution of the *in-situ* Raman experiment setup, a line scan was performed on a model device with 5 µm wide poly-c Si island electrode. The microscope image of the Si electrode is shown in Figure 3a. Raman line scans with 0.5 µm step size (limited by the focusing resolution of the microscope, ~370 nm) were performed in the direction indicated by the dashed arrow, and the collected Raman spectra are shown in Figure 3b. Based on the scanning results, the spatial resolution of this *in-situ* Raman setup is ~500 nm, as determined by the substantial drop in Si peak intensity as the laser scan reached outside the Si electrode region.

A typical Raman spectrum of poly-c Si thin electrode in the electrochemical cell is shown in Figure 3c, where three peaks were deconvoluted using Lorentzian peak fitting. The peak at ~450 cm^{-1} is attributed to ClO_4^- ion in polycarbonate solution,[34] as this peak was also observed outside the Si electrode region. The peak at ~500 cm^{-1} is attributed to undercoordinated Si atoms near the surface of poly-c Si thin film,[35] while the peak at ~520 cm^{-1} is attributed to bulk c-Si. During actual analysis of Si peak position, wavenumber below 470 cm^{-1} was truncated, then a linear background subtraction was performed, and two Lorentzian peaks were used to fit the Raman spectra.[36–38] The fitted bulk c-Si peak at ~520 cm^{-1} showed full width half maximum (FWHM) of 8 cm^{-1}, which is larger than the FWHM of Raman peak of single crystalline Si

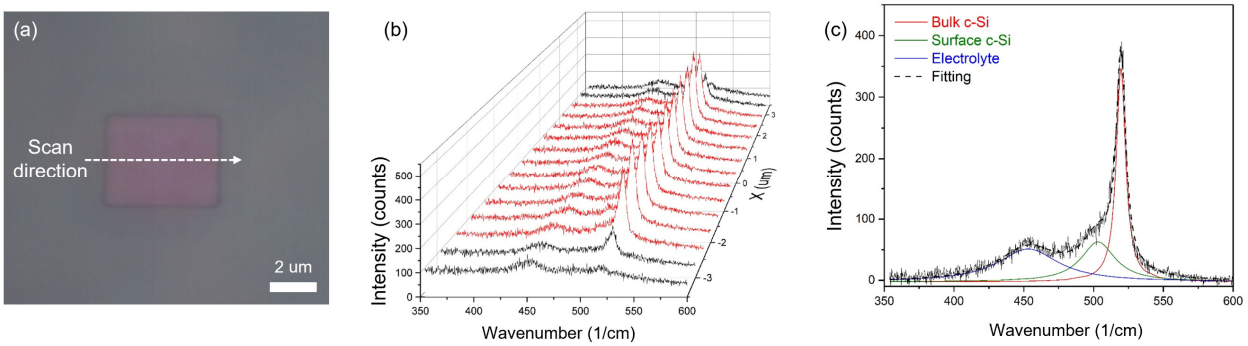

Figure 3: (a) Microscope image of Si square island with 5 µm width. (b) Raman spectra obtained from line scan (spectra colored in red correspond to poly-c Si area). (c) Raman spectrum of poly-c Si (solid black line) in the electrochemical cell, fitted by three Lorentzian peaks, and the dashed line shows the overall fitting.

(~3 cm^{-1}) and is attributed to the phonon confinement effect in the poly-c thin film.[39] Overall, the fitted spectra showed adjusted R^2 higher than 0.98, indicating a good fit.

Tungsten oxide pre-lithiation with Silicon as stress reporter

In the model electrode devices, a thin layer of tungsten oxide formed between poly-c Si and W depositions. This is evident in XRD measurement, as shown in Figure 4a (see also Figure S1 in the SI). First, the sample with only sputtered tungsten thin film was examined. This sample showed a strong diffraction peak at $2\theta \approx 40°$, corresponding to the (110) plane of α-W, while a minor peak at $2\theta \approx 35°$ was also present, attributed to the beta phase of tungsten.[40] Then, the sample with both tungsten and poly-c Si thin films showed an additional diffraction peak at $2\theta \approx 24°$, which is attributed to the oxygen deficient phase $W_{17}O_{47}$. (Phase identification from a single peak such as this is difficult, and so we refer to this phase as WO_3 in this paper for simplicity.)

The presence of WO_3 was also confirmed by electrochemical testing. In a cyclic voltammetry (CV) experiment, as shown in Figure 4b, redox peaks of tungsten oxide appeared in the potential range between 0.8 V and 1.1 V. Tungsten oxide lithiation at this potential range goes through conversion reaction,[41,42] which is typically associated with large volume change and can impose a mechanical stress on the poly-c Si overlay during electrochemical cycling. Thus, to exclude the influence of Li_xWO_3 in the following stress study of Si island electrode, a pre-lithiation step that puts Li_xWO_3 into a stable mechanical state had to be performed.

Fortunately, as seen in Figure 4b, the potential range of redox reactions is different for tungsten oxide (0.8–1.1 V) and Si (0.05–0.6 V). Thus, we selectively lithiated the tungsten oxide layer in the initial cycle, by running a linear sweep voltammetry with controlled potential between 0.3 V and 0.8 V. In this process, we first swept the potential to 0.3 V and then, held the potential for 2 hours to equilibrate lithium distribution in tungsten oxide. Subsequently, the potential was swept back to 0.8 V to finish the substrate conditioning.

The I-V curve of the pre-lithiation cycle is shown in Figure 5a, and Raman mapping at a few different potentials (Figure 5b-e) was conducted to characterize the stress response (i.e. counter stress) of the poly-c

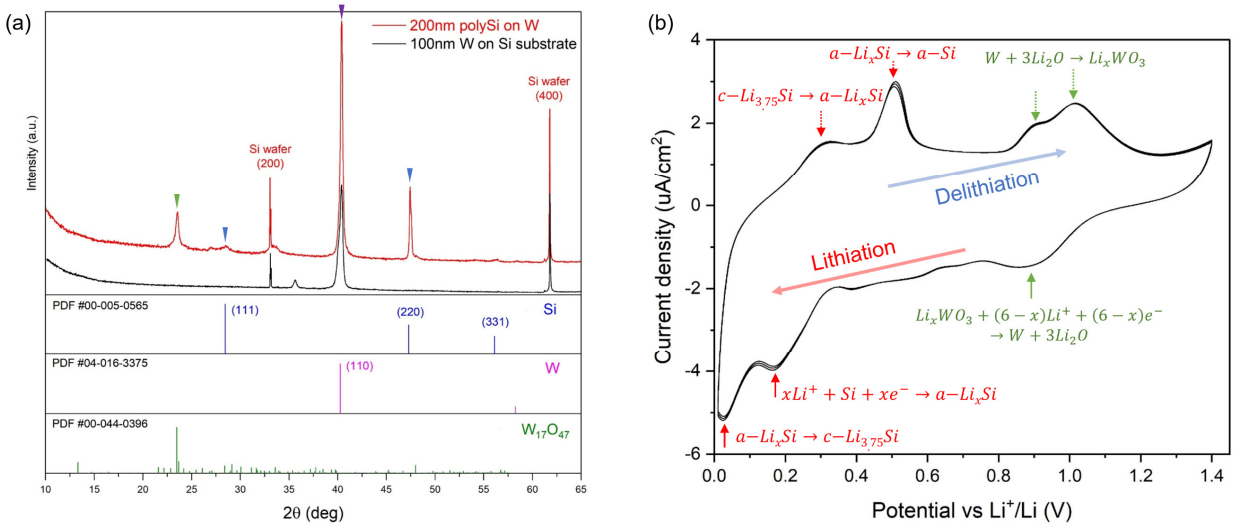

Figure 4: (a) XRD pattern of uncoated W thin film and poly-c Si/W on Si wafer substrates. (b) CV curve of poly-c Si device at potential range between 10 mV and 1.4 V annotated with electrochemical reactions for Si and WO_3.

Si layer during cycling of WO_3. As the WO_3 expands during lithiation, elastic strain is applied to the Si thin film above, resulting in a shift of the vibrational modes for Raman spectroscopy. The Raman shift is thus related to the stress state of the Si via the Young's modulus (here, the modulus of unlithiated Si, though later the modulus of lithiated Si should be used).

The diffraction peaks at $2\theta \approx 28°$ and 47° correspond to the (111) and (220) plane of c-Si, respectively. In the model electrode devices, since the majority of poly-c Si was oriented in the [110] direction, this was assumed to be the only orientation present when the Raman stress calculation was performed (see the Supporting Information for more details). The Raman shift-stress relationship is thus expressed as[43]

$$\Delta\omega = -2.3 \times \left(\frac{\sigma_x+\sigma_z}{2}\right) \quad (1)$$

Where $\Delta\omega$ is the Raman peak shift against the stress-free state, in units of cm^{-1}, and $\frac{(\sigma_x+\sigma_z)}{2}$ is the biaxial stress in poly-c Si with units of GPa. The reference wavenumber for stress-free Si is taken as 520.7 cm^{-1}, and shifts to higher wave number conventionally produce compressive stress (negative) and *vice versa*.

At open circuit potential (Figure 5b, ~2.7 V vs Li/Li^+), a stress field with small gradient was observed. The tensile stress distributed on the edge of Si electrode is attributed to the thermal expansion mismatch between WO_3 and Si layer during the deposition process. As the cell potential reached 0.4 V vs Li/Li^+, the stress gradient dramatically increased, with lithiation induced tensile stress distributed near the edge and corners of Si electrode, and the compressive stress concentrated at the center of Si electrode. The compressive stress in the center is attributed to non-uniform distribution of lithium: Li insertion into tungsten oxide proceeds through the edge beneath the Si island area, which causes volume expansion in the

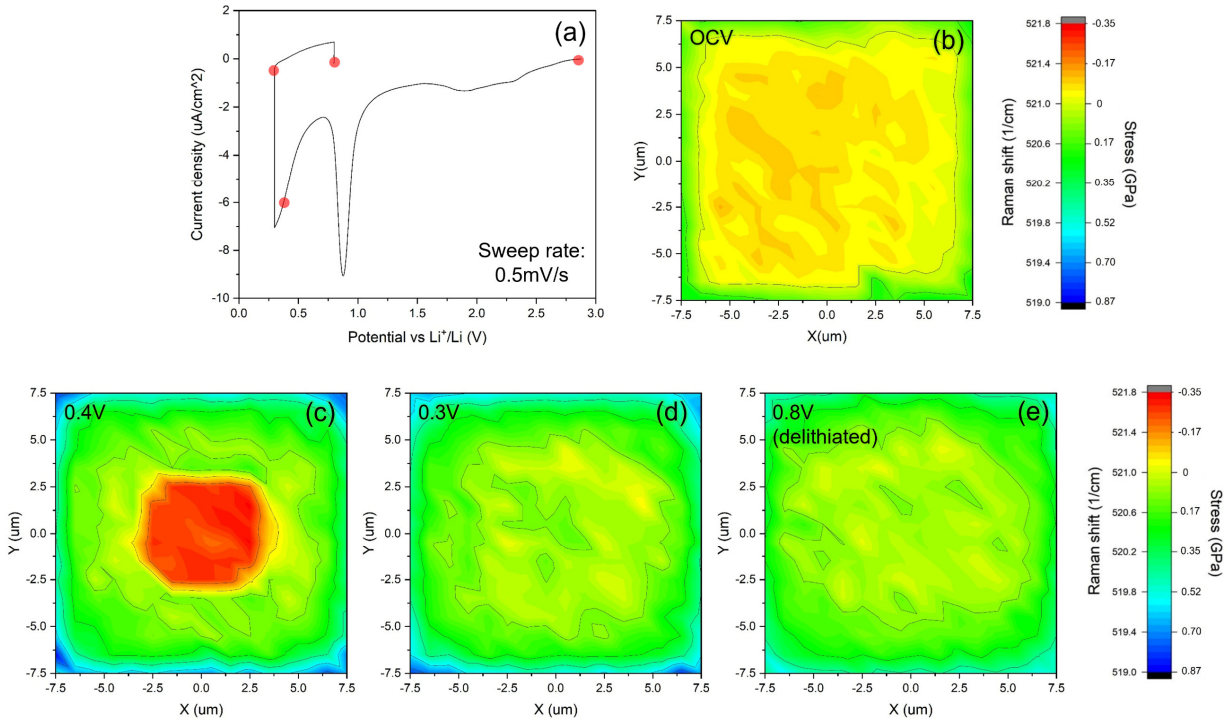

Figure 5: (a) I-V curve measured during WO_x (x≈3) substrate conditioning, with red dots indicating points at which Raman mapping was conducted. (b-e) 2D Raman stress map of Si during WO_x substrate conditioning at the indicated potentials (common color scale bar at far right).

lithiated tungsten oxide near the edge and induces compressive stress in unlithiated tungsten oxide near the center. This is reflected in the Raman stress measurement of the Si island in Figure 5c.

As lithiation proceeded to 0.3 V vs Li/Li$^+$, the stress distribution evolved to become substantially more uniform, as shown in Figure 5d, presumably due to the lithium distribution in the tungsten oxide substrate becoming more uniform. As the lithiation state of the WO_3 becomes more homogeneous, it now creates a homogeneous volume expansion, which places the majority of the Si island in tensile stress. In the following delithiation process, the cell potential was swept back to 0.8 V vs Li/Li$^+$.

No oxidation peaks were observed in this potential range in earlier CV measurements (Figure 4b), indicating the absence of electrochemical reactions, and only a broad, pseudocapacitive hump is found in Figure 5a. Consequently, the stress distribution pattern (Figure 5e) showed a very close similarity to the stress pattern at 0.3 V vs Li/Li$^+$, except the tensile stress at corners was slightly eased. At this stage, the tungsten oxide substrate remained stretched, providing a stable platform, and cycling in the Si potential range could begin.

Although the Raman stress mapping in the first cycle is notably affected by the unwanted reaction of WO_3, the good spatial resolution in the Raman mapping indicates that poly-c Si thin film could serve as a good stress reporter. Future experiments could use poly-c Si thin film as a substrate for Raman stress measurement of other electrode materials that have different operation potential range than Si.

Stress condition during Si lithiation/delithiation

After substrate conditioning in the first cycle, the Si island electrode was selectively lithiated/delithiated in the following cycle: a Li/Si half-cell was cycled between 0.15 V and 0.8 V with 0.5 mV/s rate to lithiate/delithiate the poly-c Si electrode. The corresponding I-V curve is shown in Figure 6a. The lower cut-off voltage of 0.15 V was chosen as the lowest potential for CV cycling and Raman measurement because at this potential the poly-c Si was not fully lithiated, so some crystallinity remained to produce a reasonable Raman intensity. Typically, beyond this voltage, a Si electrode becomes amorphous, though volume expansion continues. Raman spectroscopy is thus able to determine stress states only until the entire electrode becomes amorphous, and the Raman signal drops below the noise. During *in situ* measurement, any remnant crystalline Si grains are thus placed under stress from the expanding amorphous domains, and it is this stress state that we observe.

At this potential, the formation of a solid-electrolyte interface (SEI) layer from electrochemical breakdown was found to be thin enough not to block the Raman laser, i.e. 250 counts after 8 s of exposure at 0.09 mW.[7] Additionally, due to the symmetric nature of square islands, Raman line scans were performed (instead of 2D mapping) to measure stress distribution across Si islands at various potentials. The line scan

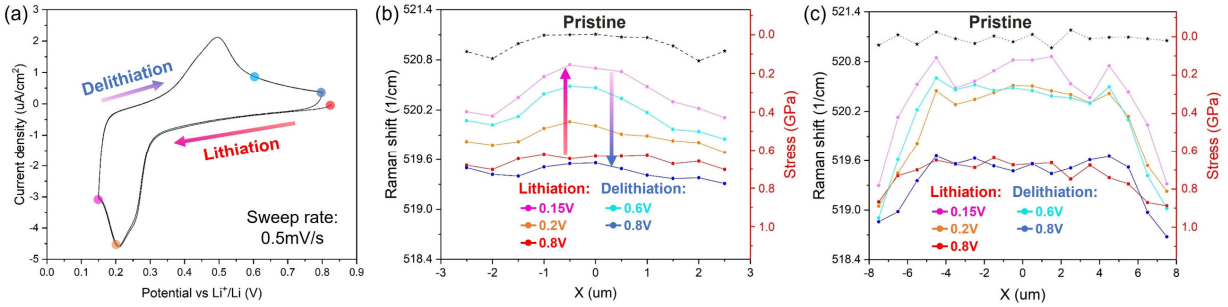

Figure 6: (a) CV curve of poly-c Si electrode at 2nd cycle (i.e. after initial substrate conditioning), with colored dots marking potentials at which the stress profile was measured. (b-c) Raman line scan of patterned poly-c Si electrodes with (b) 5 µm width, and (c) 15 µm width, with calculated stress.

results for Si island electrodes with widths of 5 μm and 15 μm are shown in Figure 6b and c. The relationship between Raman shift and stress in Si is derived in the Supplemental Information.

For Si islands with 5 μm width (Figure 6b), after substrate conditioning the poly-c Si layer first underwent a transition from a stress neutral state ("Pristine state") to a tensile stress state, i.e. at 0.8 V vs Li/Li^+ at the end of 1st cycle. The tensile stress induced by the expansion of the Li_xWO_3 layer was ~0.7 GPa. In the 2nd cycle, as the half-cell potential swept from 0.8 V vs Li/Li^+ towards lower potential, a strong reduction peak corresponding to the alloying reaction of Si occurred at ~0.2 V, and the Raman stress measurement was thus conducted at 0.2 V and 0.15 V vs Li/Li^+. At 0.2 V vs Li/Li^+, lithium insertion induced volume expansion and compressive stress in the top layer of the Si island, which partially balanced the tensile stress imposed by the preconditioned Li_xWO_3 substrate, and moved the overall tensile stress state to lower magnitude.

At 0.15 V vs Li/Li^+, the tensile stress continued to be relieved, while the center region of the Si island relaxed more than the edge, leading to a parabolic shape in the stress distribution profile, which was most pronounced at 0.15 V. In the subsequent delithiation step, the potential was swept back from 0.15 V to 0.8 V vs Li/Li^+, and the stress state of the Si island at 0.6 V and 0.8 V were measured. In this step, the stress moved back to tensile state, and the stress profile at 0.8 V at the end of 2nd cycle returned to the state at the beginning of 2nd cycle.

For the Si island electrode with 15 μm width (Figure 6c), a similar trend occurred during lithiation in which the overall stress was relaxed, although in this case a substantially steeper stress gradient developed ~3 μm away from the edge, and a prominent stress plateau formed at 0.2 V and persisted until passing 0.6 V vs Li/Li^+. The initial stress state of the Si island after prelithiation of the WO_3 current collector (0.8 V, red curve) already exhibits a small plateau ranging from 0.7–0.9 GPa. The initial stress plateau is likely caused by residual non-uniformities in the lithiation of the WO_3, possibly due to the increased diffusion lengths under the larger islands since no similar stress profile is seen at the beginning of the 5 μm Si island data (Figure 6b). During delithiation of the Si island the overall stress state moved back close to the original tensile condition, similar to the case for 5 μm Si island. This illustrates an elastic deformation mechanism, which was also observed in previous studies in this voltage range.[17] Other studies have measured plastic deformation for Si islands of this size, shown by the stress state reaching a continuous value when more deeply lithiated.[21,23]

ECM modeling and critical size effect in Si island electrode

Previously, the stress plateau and critical size of lithiated patterned Si electrode were evaluated by a shear lag model,[17,22,23] where below the critical size, the stress distribution along the lateral direction in Si electrode is a function of length and expressed as

$$\sigma_x = \frac{1}{h}\int_0^L \tau_i \, dx \tag{2}$$

where h is the height and L is half the width of the Si island electrode, and τ_i is the shearing strength of the Si/current collector interface. The stress profile predicted by the shear lag model agrees with the Raman stress measurement shown in Figure 6b. Additionally, the shear lag model predicts that the maximum stress occurs at the center of Si island, and when the width of the island goes beyond a critical value, a stress plateau arises in the center region of the island with value given as

$$\sigma_{max} = \frac{L_{crit}}{h}\tau_i \tag{3}$$

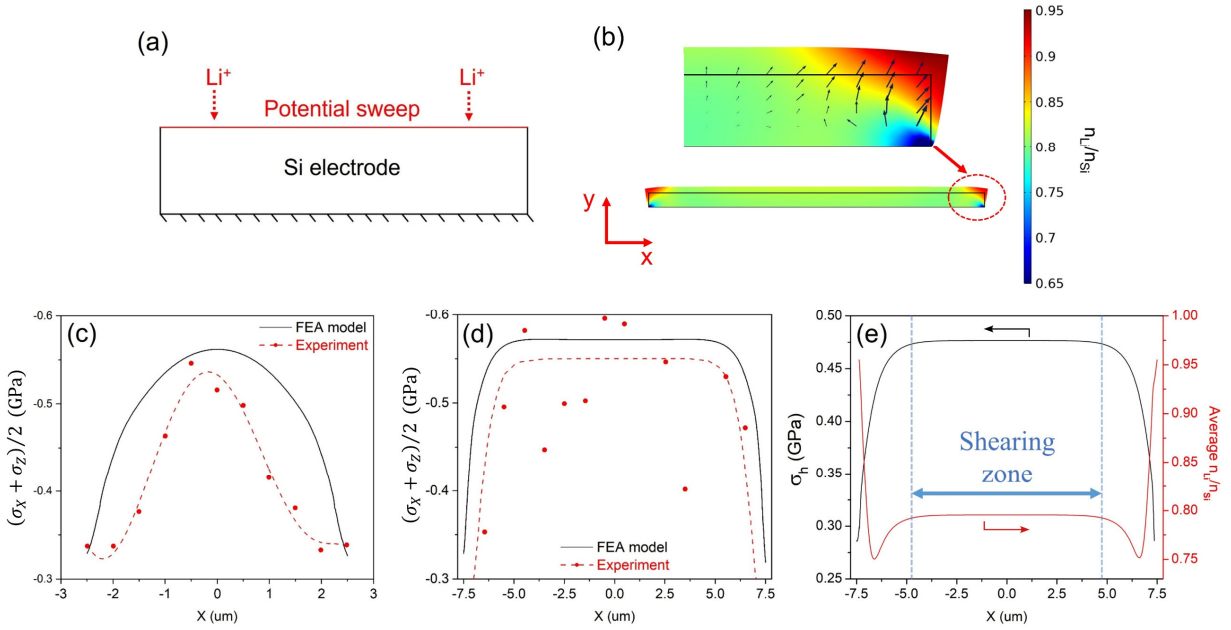

Figure 7: (a) Boundary condition and model scheme applied in FEA modeling. (b) Deformed Si electrode with 5 µm width after lithiation (black solid arrow indicates the proportional Li flux. (c) Biaxial stress profile comparison between experiment (5 µm width Si island) and modeling, and (d) comparison between 15 µm wide Si island and modeling. (e) Hydrostatic stress distribution and the associated Li concentration profile in Si electrode along x-direction.

This also agrees with the Raman stress measurement result shown in Figure 6c. In the current study, h=200 nm, and $L_{crit} \approx 5$ µm, and based on the Raman stress measurement shown in Figure 6c, $\sigma_{max} \approx 0.6\ GPa$. This leads to an assessment of the Si/W interface strength of $\tau_{i,Si/W} = 15\ MPa$, compared with a measurement of ~75 MPa from prior literature.[44]

However, the shear lag model is a pure mechanical model which describes uniaxial stress distribution in a Si island induced by external force, while in Raman measurement, an internal biaxial stress induced by lithiation in Si was measured. To model the stress profile from a physics-based model and explore the correlation between the distribution of mechanical stress and Li ion concentration, we established a 2D FEA model with coupled electrochemistry and mechanics. In this model, a plane strain condition was considered, and linear elastic deformation of the material, without plasticity, was considered under the scope of this study. The model scheme and boundary conditions are shown in Figure 7a, where a potential sweep with rate of 0.5 mV/s was applied to the top surface of Si electrode. In this way, the current density can vary across the surface of Si depending on the local state of charge and stress.

The modeled Si island electrode at 0.15 V vs Li/Li$^+$ is shown in Figure 7b, where a Li concentration gradient along the x axis is clearly shown, and edge expansion of Si electrode occurred to accommodate the mechanical stress induced by lithiation. The average amount of Li in Si predicted by the model is ~0.8 Li per Si, which is slightly lower than the calculated value, Li/Si=0.91, obtained from the CV result in Figure 6a. The difference can be explained by extra Li consumption by SEI formation in the real system.

The calculated biaxial stress, i.e. $(\sigma_x + \sigma_z)/2$, in the Si islands with different widths are shown in Figure 7c and d, which showed similar patterns to the Raman stress measurement: when the width of Si electrode is below the critical size, the biaxial stress distribution forms a parabolic profile, similar to the

experimental measurement, but as the width goes beyond the critical size, the biaxial stress reaches a plateau in the center of the geometry.

To understand the difference in the stress distribution profile associated with the width in the Si island electrode, we assessed the Li concentration and hydrostatic stress in the model in a lithiated Si electrode with size larger than the critical value, a typical distribution profile for which is shown Figure 7e. It's clear that in the center region of the Si electrode, both hydrostatic stress and Li concentration reached a plateau, while outside this region, hydrostatic stress drops, and Li concentration increases. This effect can be understood by investigating the expression for Li flux in the ECM model[45,46]

$$h_{Li} = -\mathrm{D}\left(\nabla c_{Li} - \frac{\Omega c_{Li}}{RT}\nabla\sigma_h\right) \quad (4)$$

Where c_{Li} is the Li concentration, Ω is molar volume of Li in Si matrix, σ_h is hydrostatic stress, and RT is the thermal energy. During lithiation, mechanical stress associated with Li insertion leads to a stress gradient in the lateral direction, as mechanical constraint in the center of Si is stronger than the edge. This stress gradient then drives Li to move laterally to the edge, leading to higher Li concentration at the edge than the center region.

The gradients of Li concentration and hydrostatic stress eventually reach a balanced state, forming a region in the center of Si island where stress cannot be relaxed by redistributing Li. Thus, maximum stress arises in this region, and mechanical issues such as shearing against the substrate or plastic flow in Si can occur, while outside this region, edge expansion can accommodate the excessive stress and avoid mechanical degradation in Si. Note in Figures 7c and d, the transition of stress from the center to the edges occurs over 2.5 μm in both island sizes. The stress gradient at the edge determines the size of the central plateau and is governed by the mechanical properties of the electrode, the Li diffusion coefficient and molar volume, the thickness of the island, and the boundary constraints between the electrode and the substrate. Thus, the stress plateau must be seen as a phenomenon governed by ECM coupling.

The understanding of the critical size effect here is obtained from a physics-based point of view, different from the mechanical model used in prior works.[17,22,23] The prior understanding was based solely on the mechanical properties of Si and the cohesion with the substrate, which provided an excellent foundation for the boundary conditions of the problem. In extending prior work, the model here introduces a two-way interaction between those mechanical conditions and the diffusion of Li, as in equation 4, which produces an atomistic view of the problem and doesn't rely on the specifics of the island geometry. Thus, this understanding can be applied to other dimensional systems, i.e. 1D and 3D.

Conclusion

In this work, we demonstrated an *in-situ* Raman study for stress characterization in patterned poly-c Si thin film electrodes. The experimental setup showed a high scanning resolution (~500 nm), which enabled a detailed stress study in patterned Si electrode. Tungsten oxide formation between the Si electrode and tungsten current collector caused undesired electrochemical reaction in our experiment, but this could be managed by appropriate selective cycling protocol so that significant capabilities of the technique for stress mapping under dynamic conditions have been demonstrated. By controlling the potential range of CV, we pre-lithiated the tungsten oxide layer in the initial cycle, to obtain a stably stretched substrate for later stress measurement on poly-c Si electrode. In the following CV cycles, we measured the dynamic stress change in Si at different potentials. Patterned poly-c Si electrodes with two different sizes, 5 μm and 15 μm, were studied, and the distinct stress distribution profile of those electrodes indicated different stress relaxation modes.

The experimentally measured stress plateau in the 15 μm islands (absent in the 5 μm islands) validates prior hypothesis from other groups, who inferred the stress profile based on indirect evidence. By using FEA modeling, we were able to understand the origin of different stress profiles in patterned Si electrodes and the critical size effect from a physics point of view. The model we used strongly couples Li diffusion and elastic stress, and explains the critical island size by considering that the stress plateau (caused by extrinsic boundary conditions on the free expansion of the electrode) reduces lateral Li flux, and therefore increases stress near the center of the electrode compared to islands with a smaller width. The choice of material parameters strongly affects quantitative agreement with this experiment, as does the choice of proper boundary conditions.

Our results serve to support the design of Si electrodes in fast charging battery applications. The governing equations used here that couple the Li diffusion and stress are critical to improving the modeling of Si electrode batteries using either thin film Si, Si nanoparticle additives, or porous thick film Si electrodes. While these equations have been in use for some time, experimental validation of such highly local phenomena is still lacking in the literature. Through the use of this Raman stress mapping platform, and characteristic devices such as Si island electrodes, the equations and material parameters can be confirmed. Thus, the modeling of complex, realistic systems can proceed with greater confidence.

The experimental method presented in this work shows the promise of Raman mapping in the mechanical properties study of high energy density electrodes, but much care needs to be taken to best utilize the method and interpret the results from *in-situ* Raman stress measurement. In our work, the choice of current collector, air exposure between W and Si deposition steps, and use of electrolytes that are chemically stable at the reduction potential of Si, all posed challenges. Furthermore, a small working distance for the Raman microscope and compatibility between the objective lens and electrochemical cell are critical to minimize scattering and aberrations in the Raman laser path.

We propose that crystalline Si (bulk or thin film) can be used as a promising stress reporter for Raman stress measurement of other electrode materials. While Raman stress mapping may be applied directly to other electrode materials of interest, the appropriate derivation of the Raman polarizability tensors for each crystal must be done, and relevant material properties such as the Young's modulus as a function of Li content need to be found. To date, most of this work has focused on Si electrodes, which provides a wealth of existing literature to draw from. Thus, as was done in the microelectronics industry,[47] observation of the Raman shifts in Si can be used to infer the strain states of over- or underlying layers, which can greatly expand the stress study of LIBs.

Supporting Information. EDS elemental mapping of WO_3 formation; development of finite element modeling using in this work and relevant material properties used; derivation of the relationship between Raman shift and stress for these samples.

Acknowledgement

This work was supported by the Department of Energy, Office of Science, Basic Energy Sciences, under award number DE-SC0021070. In this study, HW initiated the project, conducted experiments, and prepared the manuscript. GR and DS contributed to project initiation and guidance, data interpretation and manuscript editing. NSK, YS, VCF, PA, and SBL contributed to data interpretation and manuscript review. The authors acknowledge Don Schmadel and Nolan Ballew for helping design and fabricate

electrochemical cells and Raman testing devices. The authors also acknowledge Peter Y. Zavalij for helping fit XRD results.

Conflict of interest

The authors declare no conflict of interest.

References

(1) Jerliu, B.; Hüger, E.; Dörrer, L.; Seidlhofer, B. K.; Steitz, R.; Horisberger, M.; Schmidt, H. Lithium Insertion into Silicon Electrodes Studied by Cyclic Voltammetry and *Operando* Neutron Reflectometry. *Phys. Chem. Chem. Phys.* **2018**, *20* (36), 23480–23491. https://doi.org/10.1039/C8CP03540G.

(2) Yang, L.; Chen, H.-S.; Jiang, H.; Wei, Y.-J.; Song, W.-L.; Fang, D.-N. Failure Mechanisms of 2D Silicon Film Anodes: *In Situ* Observations and Simulations on Crack Evolution. *Chem. Commun.* **2018**, *54* (32), 3997–4000. https://doi.org/10.1039/C7CC09708E.

(3) Shi, F.; Song, Z.; Ross, P. N.; Somorjai, G. A.; Ritchie, R. O.; Komvopoulos, K. Failure Mechanisms of Single-Crystal Silicon Electrodes in Lithium-Ion Batteries. *Nat. Commun.* **2016**, *7* (1), 11886. https://doi.org/10.1038/ncomms11886.

(4) Chew, H. B.; Hou, B.; Wang, X.; Xia, S. Cracking Mechanisms in Lithiated Silicon Thin Film Electrodes. *Int. J. Solids Struct.* **2014**, *51* (23–24), 4176–4187. https://doi.org/10.1016/j.ijsolstr.2014.08.008.

(5) Wu, H.; Cui, Y. Designing Nanostructured Si Anodes for High Energy Lithium Ion Batteries. *Nano Today* **2012**, *7* (5), 414–429. https://doi.org/10.1016/j.nantod.2012.08.004.

(6) Liu, N.; Wu, H.; McDowell, M. T.; Yao, Y.; Wang, C.; Cui, Y. A Yolk-Shell Design for Stabilized and Scalable Li-Ion Battery Alloy Anodes. *Nano Lett.* **2012**, *12* (6), 3315–3321. https://doi.org/10.1021/nl3014814.

(7) Wu, H.; Chan, G.; Choi, J. W.; Ryu, I.; Yao, Y.; McDowell, M. T.; Lee, S. W.; Jackson, A.; Yang, Y.; Hu, L.; Cui, Y. Stable Cycling of Double-Walled Silicon Nanotube Battery Anodes through Solid–Electrolyte Interphase Control. *Nat. Nanotechnol.* **2012**, *7* (5), 310–315. https://doi.org/10.1038/nnano.2012.35.

(8) Liu, N.; Lu, Z.; Zhao, J.; McDowell, M. T.; Lee, H.-W.; Zhao, W.; Cui, Y. A Pomegranate-Inspired Nanoscale Design for Large-Volume-Change Lithium Battery Anodes. *Nat. Nanotechnol.* **2014**, *9* (3), 187–192. https://doi.org/10.1038/nnano.2014.6.

(9) Chan, C. K.; Peng, H.; Liu, G.; McIlwrath, K.; Zhang, X. F.; Huggins, R. A.; Cui, Y. High-Performance Lithium Battery Anodes Using Silicon Nanowires. *Nat. Nanotechnol.* **2008**, *3* (1), 31–35. https://doi.org/10.1038/nnano.2007.411.

(10) Cui, L.-F.; Ruffo, R.; Chan, C. K.; Peng, H.; Cui, Y. Crystalline-Amorphous Core−Shell Silicon Nanowires for High Capacity and High Current Battery Electrodes. *Nano Lett.* **2009**, *9* (1), 491–495. https://doi.org/10.1021/nl8036323.

(11) Liu, X. H.; Zhong, L.; Huang, S.; Mao, S. X.; Zhu, T.; Huang, J. Y. Size-Dependent Fracture of Silicon Nanoparticles During Lithiation. *ACS Nano* **2012**, *6* (2), 1522–1531. https://doi.org/10.1021/nn204476h.

(12) Ryu, I.; Choi, J. W.; Cui, Y.; Nix, W. D. Size-Dependent Fracture of Si Nanowire Battery Anodes. *J. Mech. Phys. Solids* **2011**, *59* (9), 1717–1730. https://doi.org/10.1016/j.jmps.2011.06.003.

(13) Li, J.; Dozier, A. K.; Li, Y.; Yang, F.; Cheng, Y.-T. Crack Pattern Formation in Thin Film Lithium-Ion Battery Electrodes. *J. Electrochem. Soc.* **2011**, *158* (6), A689. https://doi.org/10.1149/1.3574027.

(14) Wu, Q.; Shi, B.; Bareño, J.; Liu, Y.; Maroni, V. A.; Zhai, D.; Dees, D. W.; Lu, W. Investigations of Si Thin Films as Anode of Lithium-Ion Batteries. *ACS Appl. Mater. Interfaces* **2018**, *10* (4), 3487–3494. https://doi.org/10.1021/acsami.7b13980.

(15) Graetz, J.; Ahn, C. C.; Yazami, R.; Fultz, B. Highly Reversible Lithium Storage in Nanostructured Silicon. *Electrochem. Solid-State Lett.* **2003**, *6* (9), A194. https://doi.org/10.1149/1.1596917.

(16) Xiao, X.; Liu, P.; Verbrugge, M. W.; Haftbaradaran, H.; Gao, H. Improved Cycling Stability of Silicon Thin Film Electrodes through Patterning for High Energy Density Lithium Batteries. *J. Power Sources* **2011**, *196* (3), 1409–1416. https://doi.org/10.1016/j.jpowsour.2010.08.058.

(17) Soni, S. K.; Sheldon, B. W.; Xiao, X.; Verbrugge, M. W.; Dongjoon, A.; H., H.; Huajian, G. Stress Mitigation during the Lithiation of Patterned Amorphous Si Islands. *J. Electrochem. Soc.* **2011**, *159* (1), A38–A43. https://doi.org/10.1149/2.048201jes.

(18) Ma, Z.; Li, T.; Huang, Y. L.; Liu, J.; Zhou, Y.; Xue, D. Critical Silicon-Anode Size for Averting Lithiation-Induced Mechanical Failure of Lithium-Ion Batteries. *RSC Adv.* **2013**, *3* (20), 7398. https://doi.org/10.1039/c3ra41052h.
(19) Chen, Y.; Sang, M.; Jiang, W.; Wang, Y.; Zou, Y.; Lu, C.; Ma, Z. Fracture Predictions Based on a Coupled Chemo-Mechanical Model with Strain Gradient Plasticity Theory for Film Electrodes of Li-Ion Batteries. *Eng. Fract. Mech.* **2021**, *253*, 107866. https://doi.org/10.1016/j.engfracmech.2021.107866.
(20) Haftbaradaran, H.; Gao, H. Ratcheting of Silicon Island Electrodes on Substrate Due to Cyclic Intercalation. *Appl. Phys. Lett.* **2012**, *100* (12), 121907. https://doi.org/10.1063/1.3696298.
(21) Haftbaradaran, H.; Xiao, X.; Verbrugge, M. W.; Gao, H. Method to Deduce the Critical Size for Interfacial Delamination of Patterned Electrode Structures and Application to Lithiation of Thin-Film Silicon Islands. *J. Power Sources* **2012**, *206*, 357–366. https://doi.org/10.1016/j.jpowsour.2012.01.097.
(22) Haftbaradaran, H.; Soni, S. K.; Sheldon, B. W.; Xiao, X.; Gao, H. Modified Stoney Equation for Patterned Thin Film Electrodes on Substrates in the Presence of Interfacial Sliding. *J. Appl. Mech.* **2012**, *79* (3), 031018. https://doi.org/10.1115/1.4005900.
(23) Soni, S. K.; Sheldon, B. W.; Xiao, X.; Tokranov, A. Thickness Effects on the Lithiation of Amorphous Silicon Thin Films. *Scr. Mater.* **2011**, *64* (4), 307–310. https://doi.org/10.1016/j.scriptamat.2010.10.003.
(24) Sethuraman, V. A.; Chon, M. J.; Shimshak, M.; Srinivasan, V.; Guduru, P. R. In Situ Measurements of Stress Evolution in Silicon Thin Films during Electrochemical Lithiation and Delithiation. *J. Power Sources* **2010**, *195* (15), 5062–5066. https://doi.org/10.1016/j.jpowsour.2010.02.013.
(25) Ali, I.; Tippabhotla, S. K.; Radchenko, I.; Al-Obeidi, A.; Stan, C. V.; Tamura, N.; Budiman, A. S. Probing Stress States in Silicon Nanowires During Electrochemical Lithiation Using In Situ Synchrotron X-Ray Microdiffraction. *Front. Energy Res.* **2018**, *6*, 19. https://doi.org/10.3389/fenrg.2018.00019.
(26) Tippabhotla, S. K.; Radchenko, I.; Stan, C. V.; Tamura, N.; Budiman, A. S. Stress Evolution in Silicon Nanowires during Electrochemical Lithiation Using in Situ Synchrotron X-Ray Microdiffraction. *J. Mater. Res.* **2019**, *34* (9), 1622–1631. https://doi.org/10.1557/jmr.2019.27.
(27) Kumar, R.; Woo, J. H.; Xiao, X.; Sheldon, B. W. Internal Microstructural Changes and Stress Evolution in Silicon Nanoparticle Based Composite Electrodes. *J. Electrochem. Soc.* **2017**, *164* (14), A3750–A3765. https://doi.org/10.1149/2.0951714jes.
(28) Sethuraman, V. A.; Van Winkle, N.; Abraham, D. P.; Bower, A. F.; Guduru, P. R. Real-Time Stress Measurements in Lithium-Ion Battery Negative-Electrodes. *J. Power Sources* **2012**, *206*, 334–342. https://doi.org/10.1016/j.jpowsour.2012.01.036.
(29) Wang, H.; Kim, N. S.; Song, Y.; Albertus, P.; Lee, S. B.; Rubloff, G.; Stewart, D. Micro-Raman Stress Characterization of Crystalline Si as a Function of the Lithiation State. *ACS Appl. Mater. Interfaces* **2023**, *15* (8), 10752–10760. https://doi.org/10.1021/acsami.2c22530.
(30) Lassner, E.; Schubert, W.-D. *Tungsten: Properties, Chemistry, Technology of the Element, Alloys, and Chemical Compounds*; Springer US: Boston, MA, 1999. https://doi.org/10.1007/978-1-4615-4907-9.
(31) Sault, A. G.; Goodman, D. W. Reactions of Silane with the W(110) Surface. *Surf. Sci.* **1990**, *235* (1), 28–46. https://doi.org/10.1016/0039-6028(90)90103-F.
(32) Tompkins, H. G.; Smith, S.; Convey, D. Optimizing the Ellipsometric Analysis of a Transparent Layer on Glass. *Surf. Interface Anal.* **2000**, *29* (12), 845–850. https://doi.org/10.1002/1096-9918(200012)29:12<845::AID-SIA938>3.0.CO;2-Q.
(33) Lusty, M. E.; Dunn, M. H. Refractive Indices and Thermo-Optical Properties of Dye Laser Solvents. *Appl. Phys. B Photophysics Laser Chem.* **1987**, *44* (3), 193–198. https://doi.org/10.1007/BF00692324.
(34) Klassen, B.; Aroca, R.; Nazri, G. A. Lithium Perchlorate: *Ab Initio* Study of the Structural and Spectral Changes Associated with Ion Pairing. *J. Phys. Chem.* **1996**, *100* (22), 9334–9338. https://doi.org/10.1021/jp9537825.
(35) Gao, Y.; Yin, P. Origin of Asymmetric Broadening of Raman Peak Profiles in Si Nanocrystals. *Sci. Rep.* **2017**, *7* (1), 43602. https://doi.org/10.1038/srep43602.
(36) Teixeira, R. C.; Doi, I.; Zakia, M. B. P.; Diniz, J. A.; Swart, J. W. Micro-Raman Stress Characterization of Polycrystalline Silicon Films Grown at High Temperature. *Mater. Sci. Eng. B* **2004**, *112* (2–3), 160–164. https://doi.org/10.1016/j.mseb.2004.05.025.
(37) Pivac, B.; Furić, K.; Desnica, D.; Borghesi, A.; Sassella, A. Raman Line Profile in Polycrystalline Silicon. *J. Appl. Phys.* **1999**, *86* (8), 4383–4386. https://doi.org/10.1063/1.371374.
(38) Benrakkad, M. S.; Perez-Rodriguez, A.; Jahwari, T.; Samitier, J.; Lopez-Villegas, J. M.; Morante, J. R. Raman Characterization of Polycrystalline Silicon: Stress Profile Measurements. *MRS Proc.* **1994**, *343*, 609. https://doi.org/10.1557/PROC-343-609.

(39) Benrakkad, M. S.; Benitez, M. A.; Esteve, J.; Lopez-Villegas, J. M.; Samitier, J.; Morante, J. R. Stress Measurement by MicroRaman Spectroscopy of Polycrystalline Silicon Structures. *J. Micromechanics Microengineering* **1995**, *5* (2), 132–135. https://doi.org/10.1088/0960-1317/5/2/019.
(40) Hao, Q.; Chen, W.; Xiao, G. Beta (β) Tungsten Thin Films: Structure, Electron Transport, and Giant Spin Hall Effect. *Appl. Phys. Lett.* **2015**, *106* (18), 182403. https://doi.org/10.1063/1.4919867.
(41) Kim, J. J.; Zhou, C.; Mane, A. U.; Suh, H. S.; Kim, S.; Shi, B.; Fenter, P.; Elam, J. W.; Nealey, P. F.; Lee, B.; Fister, T. T. Structural Changes during the Conversion Reaction of Tungsten Oxide Electrodes with Tailored, Mesoscale Porosity. *ACS Nano* **2022**, *16* (4), 5384–5392. https://doi.org/10.1021/acsnano.1c08599.
(42) Zheng, M.; Tang, H.; Hu, Q.; Zheng, S.; Li, L.; Xu, J.; Pang, H. Tungsten-Based Materials for Lithium-Ion Batteries. *Adv. Funct. Mater.* **2018**, *28* (20), 1707500. https://doi.org/10.1002/adfm.201707500.
(43) Wolf, I. D. Micro-Raman Spectroscopy to Study Local Mechanical Stress in Silicon Integrated Circuits. *Semicond. Sci. Technol.* **1996**, *11* (2), 139–154. https://doi.org/10.1088/0268-1242/11/2/001.
(44) Son, S. J.; Park, K. H.; Katoh, Y.; Kohyama, A. Interfacial Reactions and Mechanical Properties of W–SiC in-Situ Joints for Plasma Facing Components. *J. Nucl. Mater.* **2004**, *329–333*, 1549–1552. https://doi.org/10.1016/j.jnucmat.2004.04.285.
(45) Zhang, X.; Shyy, W.; Marie Sastry, A. Numerical Simulation of Intercalation-Induced Stress in Li-Ion Battery Electrode Particles. *J. Electrochem. Soc.* **2007**, *154* (10), A910. https://doi.org/10.1149/1.2759840.
(46) Xu, R.; Zhao, K. Electrochemomechanics of Electrodes in Li-Ion Batteries: A Review. *J. Electrochem. Energy Convers. Storage* **2016**, *13* (3), 030803. https://doi.org/10.1115/1.4035310.
(47) Wolf, I. D. Stress Measurements in Si Microelectronics Devices Using Raman Spectroscopy. *J. Raman Spectrosc.* **1999**, *30* (10), 877–883. https://doi.org/10.1002/(SICI)1097-4555(199910)30:10<877::AID-JRS464>3.0.CO;2-5.